73nd International Astronautical Congress (IAC), Paris, France, 18-22 September 2022.

IAC-22-C1.IPB.26.x71391

Sensitivity analysis of asteroid ejecta models for future in-orbit sample collection mission

Mirko Trisolini[a]*, Camilla Colombo[a], Yuichi Tsuda[b]

[a] *Department of Aerospace Science and Technology, Politecnico di Milano, via La Masa 34, 20156, Milano, Italy,* mirko.trisolini@polim.it
[b] *Institute of Space and Astronautical Science (ISAS)/Japan Aerospace Exploration Agency (JAXA)*, 3-1-1 Yoshinodai, Chuo-ku, Sagamihara, Kanagawa 252-5210, Japan, tsuda.yuichi@jaxa.jp
* Corresponding Author

Abstract

This work presents a sensitivity analysis on ejecta models used to model impact events onto small bodies in the Solar System. The application in exam is focused on kinetic impacts on Near Earth Asteroids to study the possibility of collecting the generated fragments in orbit, thus avoiding landing or touchdown operations. The sensitivity analysis shown in this work is articulated in three phases. A first analysis that studies the effect of the impactor and target properties on the overall fate of the ejecta. A second analysis that focuses on quasi-stable orbits: here we estimate the number of particles expected to be trapped into quasi-stable orbits depending on the impact location and the characteristics of the impact event. A third and final phase that focuses on a numerical methodology to predict the flux of impacts on a spacecraft positioned around the asteroids. This allows the estimate of the number of collectable particles by the spacecraft as a function of its position. For each one of these analyses, we study their sensitivity to different aspects of the ejecta model.

Keywords: asteroids, ejecta, sensitivity analysis, sample collection, photo-gravitational Hill problem

1. Introduction

Asteroids carry fundamental information on the evolution of our Solar System. They are rich in valuable resources, which could be exploited through future asteroid mining missions, and enable long-duration missions self-sustaining. Our knowledge of the physical composition of asteroids can be significantly improved by collecting and studying their samples, thus better targeting asteroids for material exploitation or increasing the efficiency of asteroid deflection missions. One of the most challenging aspects of scientific missions at asteroids is to collect and sample asteroid material by means of an on-ground collection, involving landing (or touchdown) and mining. In the context of future asteroid exploration missions, within the Collecting Asteroid-Orbiting Samples - CRADLE project, funded by the Horizon 2020 MSC Actions, we envision the possibility to perform in-orbit collection as an alternative to landing or touchdown operations [1][2][3].

This work presents the development of a statistical ejecta model by means of probability density functions. These distribution functions are used to model the ejecta in terms of particle size, launch location, ejection velocity, and ejection direction, to model the outcome of an impact of a small kinetic impactor onto asteroid surfaces. The parameters defining the models are determined by the characteristics of the target and the impactor and are computed based on experimental correlations and conservation laws.

As the aim of the CRADLE project is to verify the collectability of particles generated by small kinetic impactors, it is important to understand the sensitivity of the ejecta models from both the impact conditions and the modelling assumptions.

In this work we study the sensitivity of the ejecta fate with respect to different aspects and parameters of the ejecta model. Section 4.1 shows a simplified analysis of the overall fate of the ejecta as a function of the target and impactor properties. Section 4.2 studies the effect of the target material type and strength, as well as the impact location, on the possibility of the generated fragments to be trapped into quasi-stable orbits. Section 5 describes a numerical analysis devoted to the estimation of the fragments' flux on a spacecraft orbiting the asteroid in order to estimate the possible number and characteristics of collectable particles by an in-orbit sample collection mission.

2. Sensitivity analyses

This work is focused on assessing the sensitivity of the ejecta generation and propagation processes. We perform this analysis at different level of details as follows:

1. First, we look at the overall fate of the ejecta by checking the fraction of fragments that could be available for collection based only on their initial conditions. This analysis is carried out varying

the target and impactor characteristics to understand the sensitivity to these parameters.

2. Second, we focus on quasi-stable orbits. Fragments in these orbits can perform more the one revolution around the asteroid. As such, they could allow for a better collection alternative, given the longer time the spacecraft has to collect them. In this work, we estimate the number of fragments in quasi-stable orbits as function of the impact location and the impact conditions.
3. Third, a numerical analysis aimed at estimating the flux of fragments around the asteroid. Estimating the flux can also allow the estimate of the number of fragments a spacecraft can intercept as a function of its position in time. The methodology we employ here is based on a weighted Monte Carlo technique. Therefore, we verify its sensitivity and stability with respect to the number of samples and realisations.

The following sections describes the methodologies and results obtain for the aforementioned analyses. The test case for this study is asteroid Ryugu, whose main characteristics can be found in Table 1. These will represent the average target characteristics.

Table 1: Characteristics of asteroid Ryugu [4].

Quantity	Symbol	Value
Mean radius (m)	R_a	440
Bulk density (g/cm3)	ρ	1.19
Albedo	C_r	0.037
Rotational period (h)	T_r	7.627

The average impactor characteristics are also derived from the mission Hayabusa2 [4][5] and are summarised in Table 2.

Table 2: Impactor properties [4][5].

Quantity	Symbol	Value
Speed (km/s)	U	2
Radius (m)	a	0.075
Density (g/cm^3)	δ	2.7

Finally, the two materials considered in the study are a sand-like, strengthless material, and the Weakly Cemented Basalt (WCB) material, at three different strength levels (10, 1000, and 10000 Pa, respectively). Table 3 summarises the properties of the materials.

Table 3: Ejecta models material parameters [6].

	Sand	WCB
K_1	0.24	0.24
μ	0.41	0.46
C_1	0.55	0.18
k	0.3	0.3
H_1	0.59	-
H_2	-	0.38
n_1	1.2	1.2
Y_{ref} (MPa)	0	0.45

First, however, we provide a description of the ejecta model that is used throughout the study.

3. Ejecta distribution model

The ejecta model describes the characteristics of the ejected particles after an impact that is the particle size, s, ejection speed, u, and launch direction, ξ and ψ. Specifically, we will use the ejecta model to describe the effect of an impact with a small kinetic impactor, comparable to the one of the Hayabusa2 mission [5].

The ejecta model we used is defined using a continuous density function of the form [2]:

$$p(s,r,\xi,\psi) = p_s(s)\cdot p_{\psi|\xi r}(\psi|\xi,r;\phi) \cdot p_{\xi|r}(\xi|r;\psi)\cdot p_r(r), \quad (1)$$

where s is the particle radius, r the launch location inside the crater, ξ the in-plane launch angle, ψ the out-of-plane launch angle (Figure 1), and ϕ is the impact angle (measured from a plane tangent to the asteroid at the impact point).

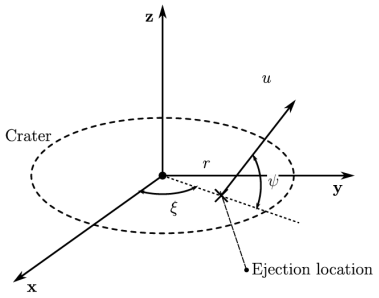

Figure 1: Schematics of the parameters defining the ejecta conditions with respect to a reference frame tangent to the surface of the asteroid at the impact point.

As Eq. (1) shows, a generic ejection distribution can be expressed as a combination of conditional distribution functions that depend on the impact angle. Specifically, p_s is the distribution function of the particle size, $p_{\psi|\xi r}$ is the conditional distribution function of the out-of-plane ejection angle given the in-plane angle and the launch position, $p_{\xi|r}$ is the conditional distribution of the in-plane ejection angle given the launch location, and p_r is the distribution of the launch location. The expressions for the single distributions are as follows:

$$p_s(s) = \bar{\alpha} N_r s^{-1-\bar{\alpha}} \quad (2)$$

where $\bar{\alpha}$ defines the slope of the power law and N_r is a constant determined from mass conservation and is equal to:

$$N_r = \frac{3(3-\bar{\alpha})M_{tot}}{4\bar{\alpha}(s_{max}^{3-\bar{\alpha}} - s_{min}^{3-\bar{\alpha}})\pi\rho} \tag{3}$$

where M_{tot} is the total ejected mass from the crater [2], and s_{min} and s_{max} are the minimum and maximum particle radii, respectively.

$$p_r(r) = \frac{3k\rho}{M_{tot}} r^2 \quad \text{with } r_{min} \leq r \leq r_{max} \tag{4}$$

where k is a scaling parameter depending on the target material (see Table 3). The launch location, r, is directly correlated to the ejection speed as follows [7][8]:

$$u(r) = C_1 \cdot U \cdot \left[\frac{r}{a} \cdot \left(\frac{\rho}{\delta}\right)^{\nu}\right]^{-\frac{1}{\mu}} \cdot \left(1 - \frac{r}{r_{max}}\right)^{p} \tag{5}$$

Where U is the impactor speed, δ the impactor density and a is the impactor radius. The coefficients C_1, μ, ν, and p, are parameters depending on the material (see Table 3). The parameter $r_{max} = n_2 \cdot r_c$ is connected to the crater radius (r_c) and the coefficient n_2, which depends on the type of material (see Table 3). The crater radius can be computed following Housen expression as follows [7]:

$$r_c = \frac{3mK_1}{\pi\rho}\left(\frac{ga}{U^2}\left(\frac{\delta}{\rho}\right)^{\frac{1}{3}} + \left(\frac{Y}{\rho U^2}\right)^{\frac{2+\mu}{2}}\right)^{-\frac{\mu}{2+\mu}} \tag{6}$$

Where m is the impactor mass, g the gravitational acceleration at the surface of the target asteroid, Y the equivalent strength of the target material and K_1 is a constant dependent on the target material.

The in-plane ejection angle has the following expression which derived from the work of Richardson [12]:

$$p_{\xi|r}(\xi|r) = \frac{1}{2\pi}\left[1 - \cos\phi\left(\cos 2\xi \cos^3\xi - \frac{1}{5}\cos\xi\cos^4 2\xi\right)\left(1 - \frac{r^8}{r_{max}^8}\right)\right] \tag{7}$$

Figure 2 shows an example of the variation of the in-plane ejection angle distribution of Eq. (7) as function of the impact angle, for a fixed launch location, r.

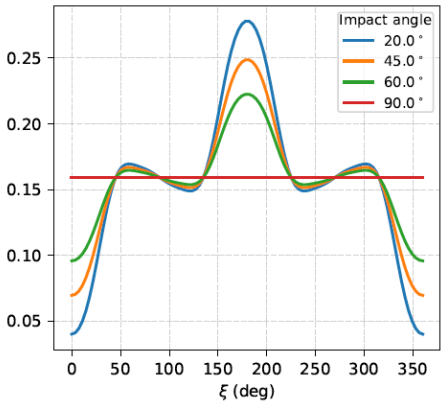

Figure 2: In-plane ejection angle conditional distribution for different impact angles and a fixed launch location, r.

The out-of-plane ejection angle is modelled using a gaussian distribution as follows:

$$p_{\psi|\xi,r}(\psi|\xi, r; \phi) = \mathcal{N}(\mu_n - K_\psi, \sigma_n) \tag{8}$$

where μ_n and σ_n are the mean and standard deviation of ψ for a normal impact (impact with a 90° angle with respect to the local horizontal plane) and can be derived from experimental correlations:

$$\begin{cases} \mu_n = \mu_0 - \mu_d \cdot r/r_{max} \\ \sigma_n^2 = \sigma_0^2 + \sigma_d^2 \cdot \left(\frac{r}{r_{max}}\right)^2 \end{cases} \tag{9}$$

where $\mu_0 = 52.4°$, $\sigma_0 = 3.05°$, $\mu_d = 18.4°$, and $\sigma_d = 4.1°$, respectively [12]. The constant K_ψ has the following expression:

$$K_\psi = \frac{\pi}{6}\cos\phi\left(\frac{1-\cos\xi}{2}\right)\left(1 - \frac{r}{r_{max}}\right)^2 \tag{10}$$

Figure 3 shows an example of the out-of-plane ejection angle distribution for a fixed r and varying in-plane ejection angles, for a 45° impact angle.

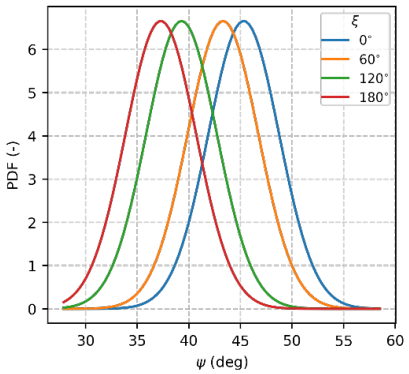

Figure 3: Example of conditional out-of-plane ejection angle distribution for an impact at 45° impact angle.

For a more detailed description of the model, the reader is referred to [2].

To define the distribution, it is necessary to specify the properties of the target and the impactor, as well as the characteristics and range of validity of the distributions. Throughout this work, the following assumptions holds:

- The minimum particle radius, s_{min}, is equal to 10 μm [9].
- The maximum particle radius, s_{max}, is equal to 1 cm for sand-like materials and 10 cm for WCB [9].
- The launch location, r, ranges between the inner and outer rim of the crater formed by the impact. In the following analyses, we limit the ejection speed to the escape speed of the asteroid, therefore, we also limit the minimum launch location to the one corresponding to the escape speed.
- The slope of the particle size distribution, $\bar{\alpha}$, is 2.4 in all cases [10].

4. Analytical Analysis

This section presents a sensitivity study performed using analytical methodologies. In Section 4.1, we only look at the initial conditions of the ejection and exploit the characteristics of the distribution-based ejecta model to estimate the number of particles satisfying specific conditions. In Section 4.2, instead, we look at what conditions can lead to quasi-stable orbits. We estimate how many particles are injected into these stable orbits depending on the target and impact characteristics, and the impact location.

4.1 Effect of target and impactor properties

In this analysis, we look at two extreme conditions. Specifically, initial conditions leading to fragments not reaching a sufficient height to be collected and conditions leading to a quick escape from the system. For the first condition, we selected an altitude of 50 m. From this limit we derive a minimum speed, considering, for simplicity, a purely ballistic flight.

$$u_{min} = \sqrt{\frac{2gh_{max}}{\sin^2 \psi}} \tag{11}$$

where h_{max} = 50 m and ψ = 45°. For the second condition, the escape speed of the asteroid as function of the particle size is considered [16]

$$u_{max} = \sqrt{\frac{2\mu_a}{R_a} - \frac{d}{\mu}\sqrt{\frac{\mu_a}{G_1}\cdot\frac{m_p}{A_p}}} \tag{12}$$

where μ_a is the gravitational parameter of the asteroid, d is the Sun-asteroid distance, m_p is the particle mass, A_p is the particle cross-section, and G_1 is the SRP strength parameter [16].

From the two velocity limits we can obtain the radius limits inverting Eq. (5), so that we can integrate the Cumulative Distribution Function (CDF) of Eq. (4). The integral of the distribution can return an estimate of the number of particles satisfying these conditions. We consider that particles with speed outside the aforementioned range cannot be collected, while the ones inside are available and a strategy can be devised to collect. This procedure is to have an estimate of the amount of fragments available and assess their sensitivity to the target and impactor properties.

4.1.1 Target sensitivity

In this section we study the sensitivity to the target. Assuming as nominal properties the ones of Ryugu defined in Table 1 we vary:

- material type and strength: sand-like and Weakly Cemented Basalt (WCB) materials with varying strengths
- asteroid density: ∓20% nominal value [17]
- asteroid size: ∓10% nominal value [17]

Figure 4 shows the boxplot of the fraction of particles having a maximum altitude below 50 meters. We can observe that the fraction of particles changes significantly with the material strength and decreases as the strength increases.

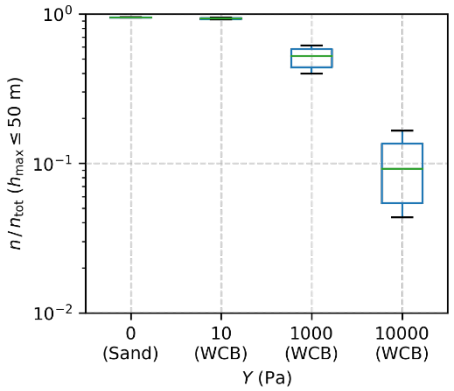

Figure 4: Boxplot of the fraction of particles having maximum altitude below 50 m as a function of the material type and strength.

For the very low strength options, almost 90% of the particles do not reach altitudes grater than 50 m. We can

also observe that the effect of the target characteristics grows with the material strength as a higher variability is observed.

Figure 5 shows an equivalent boxplot for the particles quickly escaping the system. The behaviour here is opposite to Figure 4 but still influenced by the material type and strength. The sensitivity to the target properties is instead lower as it is observed by the size of the boxplot. Finally, Figure 6 shows the total number of fragments ejected between the velocity limits of Eq. (11) and (12). We observe that the influence of the material type and strength is greater than the uncertainty in the target property. We also observe, as expected, that the greater the strength, the lower the amount of available fragments. However, in all cases, a number of fragments in the order of billions is potentially available for collection.

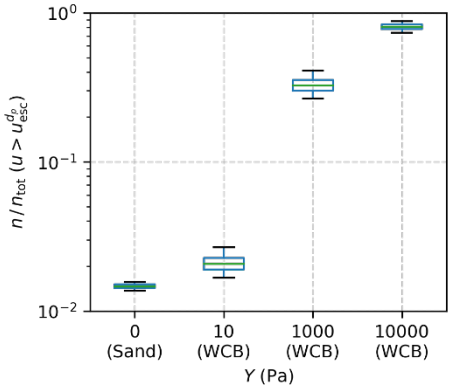

Figure 5: Boxplot of the fraction of particles quickly escaping the system as a function of the material type and strength.

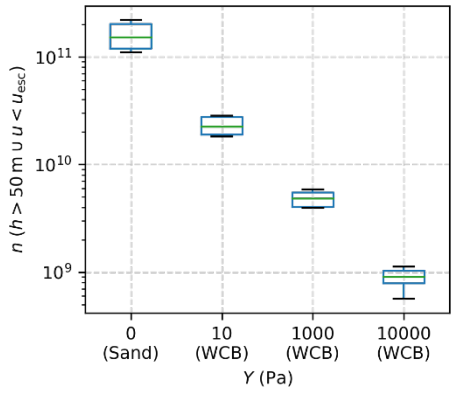

Figure 6: Boxplot of the number of fragments *potentially available* for collection as a function of the material type and strength.

4.1.2 Impactor sensitivity

In this section, instead, we look at the influence of the impactor. Specifically, we vary the impactor speed, U, size, a, and density, δ, as follows:

- $U \in \{500, 1000, 2000, 3000\}$ m/s
- $a \in \{0.05, 0.075, 0.1, 0.15\}$ cm
- $\delta \in \{500, 1000, 2000, 3000\}$ kg/m^3

Figure 7 shows the fraction of particles escaping the system and their variability as function of the impact properties. We can observe that the effect of the impactor properties is of a few percent difference for low strength materials and increases to around 10% as the material strength increases (notice the scale of the plot is logarithmic). Figure 8 shows the boxplot of the total number of *available* fragments. As in Figure 6, the amount of fragments decreases with increasing strength. In addition, we observe a much larger variability with respect to the impactor properties, as opposed to the target. A first reason is the larger range of variability we chose for the impactor properties. A second reason is the influence of the impactor speed on the crater diameter: the higher the impact speed the bigger the crater and the larger is the amount of fragments. Varying from 500 to 3000 m/s the impact speed generates higher variations in the number of ejected fragments.

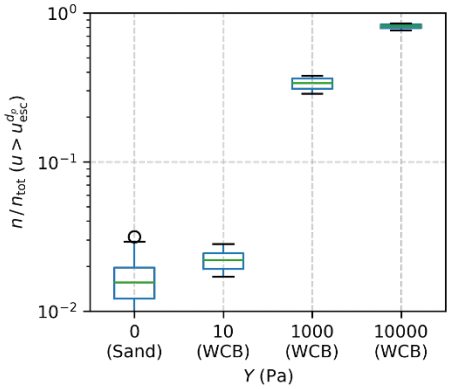

Figure 7: Boxplot of the fraction of particles quickly escaping the system as a function of the material type and strength.

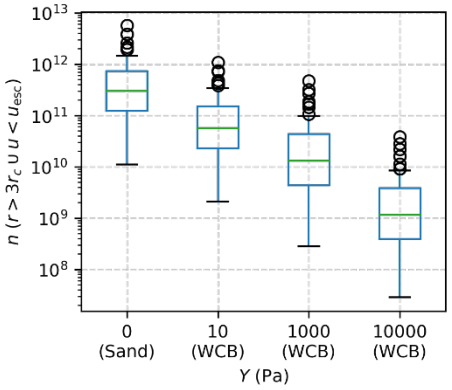

Figure 8: Boxplot of the number of fragments *potentially available* for collection as a function of the material type and strength.

4.2 Quasi-stable orbit analysis

In this section, we present an analysis that exploits the ejecta model described in Section 3 in a different fashion. Specifically, we want to identify those initial conditions that lead to quasi-stable orbits and then estimate how many particles can be trapped into these orbits as a function of the impact conditions.

To find the initial conditions leading to such orbits, we exploit the analytical solution by Richter [15]. Richter gives the analytical solution to a particle orbit evolution around a spherical body moving on an elliptical orbit around the Sun, considering the contribution of solar radiation pressure. The contribution of the third body effect and the irregularities of the gravity field of the small body are instead neglected. The averaged equation of motion in a reference frame centred in the asteroid and moving with it are as follows:

$$\begin{aligned} L_{0x} &= -\frac{c_2}{k}cos\psi + \frac{c_3}{k}sin\psi + \frac{c_1 k_0}{k} \\ L_{0y} &= c_2 sin\psi + c_3 cos\psi \\ L_{0z} &= \frac{c_5 k_0}{k}cos\psi - \frac{c_6 k_0}{k}sin\psi + \frac{c_4}{k} \\ x_{m0} &= -\frac{c_5}{k}cos\psi + \frac{c_6}{k}sin\psi + \frac{c_4 k_0}{k} \\ y_{m0} &= c_5 sin\psi + c_6 cos\psi \\ z_{m0} &= \frac{c_2 k_0}{k}cos\psi - \frac{c_3 k_0}{k}sin\psi + \frac{c_1}{k} \end{aligned} \tag{13}$$

Where c_1 to c_6 are constants that depend on the initial conditions and

$$\begin{aligned} k &= \sqrt{k_0^2 + 1} \\ \psi &= k(\varphi - \varphi_0) \end{aligned} \tag{14}$$

where φ is true anomaly of the asteroid along its orbit and φ_0 is the initial true anomaly. Additionally, we have:

$$k_0 = \frac{3}{2}\left[\frac{M_s}{M_a a_a (1 - e_a^2)}\right]^{\frac{1}{2}} a^{1/2}\beta \tag{15}$$

Where M_s is the mass of the Sun, M_a the mass of the asteroid, a_a and e_a the semi-major axis and eccentricity of the asteroid's orbit around the Sun, β the lightness parameter and a is the semi-major axis of the particle's orbit around the asteroid. In Eq. (13), L_0 and x_m are the normalised angular momentum and apocentre direction. The normalisation has the following expressions:

$$\begin{aligned} \boldsymbol{L_0} &= \frac{\boldsymbol{L}}{M_p\sqrt{\mu_a a}} \\ \boldsymbol{x_{m0}} &= \frac{2}{3a}\cdot \boldsymbol{x_m} \end{aligned} \tag{16}$$

Where M_p is the mass of the mass of the particle. Given the initial conditions of the ejection in terms of ejection location (right ascension and declination with respect to a frame moving with the asteroid and centred in it), particle size, ejection speed, and ejection direction, we can compute the corresponding initial conditions in terms of L_0 and x_{m0}. Using the initial conditions, we can solve the system of Eq. (13) for the constants c_1 to c_6. Once we have the constants, we know the evolution of the particle's orbits as a function of the true anomaly of the asteroid along its orbit.

With this methodology, we check the evolution of the particle's orbit eccentricity. Once the eccentricity grows above a critical eccentricity, e_c, the particle is considered to impact the asteroid. To verify that an orbit is quasi-stable, we evaluate the eccentricity at time intervals of a period of the orbit and compare it with the critical eccentricity. If the particle performs at least one revolution is considered to be quasi-stable.

$$e(T) < e_c = 1 - \frac{R_a}{a} \tag{17}$$

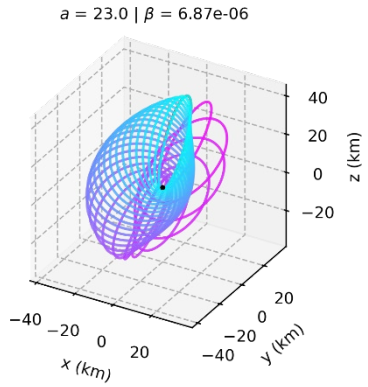

Figure 9: Example of quasi-stable orbit.

As this methodology is analytical it allows to check a large set of initial conditions. Specifically, in this study, we perform a vast grid search. First, we consider a grid of ejection location in right ascension and declination, subdividing the right ascension every 45° and the declination every 15°. Then for each impact location. We perform a grid search in the particle size, speed, and ejection direction. We consider a size range between 0.5 mm and 10 cm, subdivided in 40 bins. The in-plane ejection angle, xi, is considered between 0° and 360° and subdivided in 24 intervals, while the out-of-plane ejection angle is between 5° and 85° for a total of 8 bins. Finally, the ejection speed has a maximum that depends on the particle size according to Eq. (12) and is subdivided into 60 bins. A total of over 30 million initial conditions have been checked for quasi-stable orbits.

Figure 10 shows the average orbiting time for quasi-stable orbits generated from different ejection location.

We observe that the mean orbiting time ranges from about 10 days to about 50 days. The peak orbiting time is obtained for impact location with zero right ascension and declination, i.e., the anti-solar direction, while the lower times are at the solar pointing location. We also observe a slight asymmetry with longer orbiting times for particles ejected from positive right ascension. Figure 11 shows the average ejection speed that leads to quasi-stable orbits for different ejection locations. It is possible to observe the antisymmetric behaviour of the speed, due to the contribution of the rotation of the asteroid, where higher ejection speeds are required for positive right ascensions.

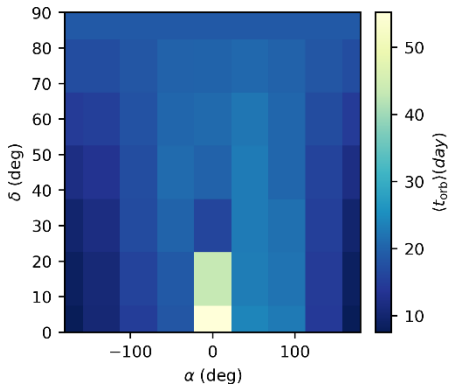

Figure 10: Average orbiting time for quasi-stable orbit as function of the impact location.

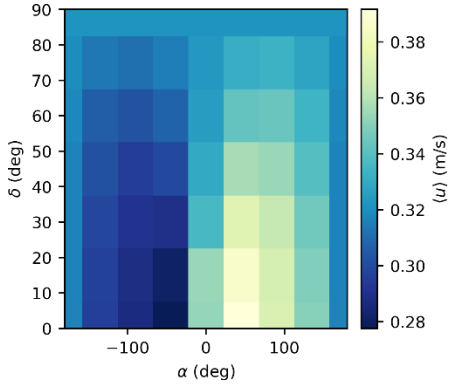

Figure 11: Average ejection speed for quasi-stable orbits as function of the ejection location

Figure 12 shows the average number of pericentre passages of the quasi-stable orbits. We can observe that polar orbits tend to perform more "revolutions", as well as orbits ejected perpendicular to the Sun-asteroid line. For each ejection location we have a series of initial conditions that lead to quasi-stable orbits. These initial conditions are expressed in the synodic frame. If we apply a transformation to consider the contribution of the asteroid rotation, we can obtain the same initial conditions in the local horizontal frame.

$$\boldsymbol{v} = \boldsymbol{v}_{syn} - \boldsymbol{v}_{rot}(\alpha, \delta) \tag{18}$$

Where $\boldsymbol{v}_{syn}$ is the speed in the synodic frame (the original speed used in the Richter equations) and $\boldsymbol{v}_{rot}$ is the rotational speed of the asteroid at the ejection location.

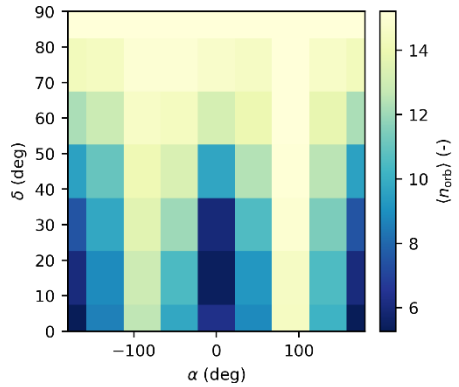

Figure 12: Average number of pericenter passages as function of the ejection location.

At that point, it is possible to compare these initial conditions with the ejecta distribution model described in Section 3. Specifically, we can define a four-dimensional volume in the s, r, ξ, ψ space and we can integrate the distribution of Eq. (1) in this volume. The volume can be schematised simply creating a four-dimensional histogram in the aforementioned states space and identify the bins with at least one initial condition that leads to quasi-stable orbits. The ensemble of these bins approximates the "volume" of initial conditions for quasi-stable orbits. Note that we need to transform the initial conditions of the ejection speed, u, into launch position, r. Therefore, we can estimate the number of particles as

$$n_f(\alpha, \delta) = \sum_{i=1}^{N} q_i \cdot \int_{dV_i} p(s, r, \xi, \psi) \tag{19}$$

Where N is the total number of bins subdividing the state space of initial conditions and dV_i is the volume of the i-th bin. The parameter q_i is a 0-1 switch; is 1 if the bins contain conditions leading to quasi-stable orbits and is 0 in the other case. Therefore, all the bins with $q_i = 0$ are not considered in the integral (Figure 13).

Figure 14 shows the estimated number of fragments injected into quasi-stable orbits from different ejection locations. The plot is obtained using an ejection distribution relative to a normal impact onto sand-like terrains. We can observe a large central area ranging from -45° to +45° in right ascension and up to 60° in declination for which no fragments belong to quasi-stable orbits. As previously show, this area has initial conditions that lead to quasi-stable orbits; however, these initial

conditions fall outside the actual ejection distribution. Specifically, from these locations, only particles larger than 1 cm can be trapped into quasi-stable orbits. However, we modelled the sand-like material with an upper limit of 1 cm in particle diameter. We then observe a fairly symmetrical behaviour, with peak number of fragments for orbits starting from location on the Sun side.

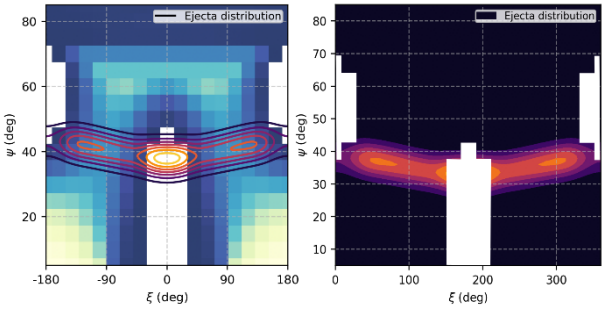

Figure 13: Simplified representation of the procedure to estimate the number of fragments in quasi-stable orbits. Here only the subset of variable of the ejection angle is shown. On the left, the blue shaded area represents regions leading to quasi-stable orbits, while the contours represent the ejecta distribution for a 45° impact. On the right, we show the portion of the ejecta distribution that are integrated.

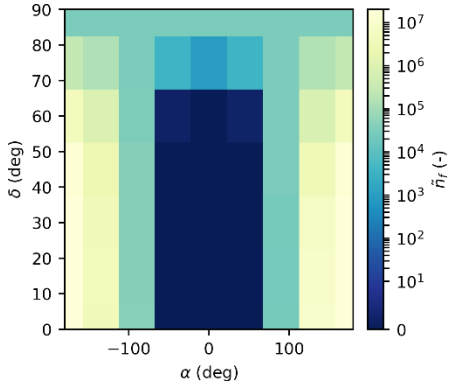

Figure 14: Estimated number of fragments in quasi-stable orbits as function of the ejection location for a normal impact on a sand-like target material.

Similarly, Figure 15 shows the estimated number of fragments injected into quasi-stable orbits from different ejection locations. In this case, the plot is obtained using an ejection distribution relative to a normal impact onto WCB material with a 10 kPa equivalent strength. The behaviour of Figure 15 is analogous to Figure 14; however, we observe two differences. First, the central region now shows particles in quasi-stable orbits. For this material, in fact, the upper limit of the particle diameter is 10 cm. Second, the total number of fragments is lower than the sand-like case. In fact, in general, sand-like terrains bigger crater and thus more fragments. However, this difference is only of one order of magnitude, while the total number of fragments ejected in the sand-like case is three orders of magnitude higher than the WCB case at 10 kPa. Therefore, the number of fragments into quasi-stable orbits may be less influenced by the strength of the target material.

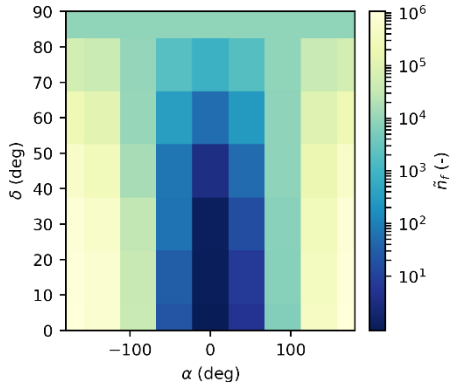

Figure 15: Estimated number of fragments in quasi-stable orbits as function of the ejection location for a normal impact on a WCB target material with equivalent strength of 10 kPa.

5. Numerical analysis

5.1 Dynamical model

The dynamical model used in this work is the Photo-gravitational Hill Problem [13][14]. We neglect the irregularities of the gravity field as we are mainly interested in the sensitivity of the flux and impact estimation methodology to the sampling technique.

The equations of motion are expressed in non-dimensional form in a synodic reference frame centred in the asteroid. The x-axis is along the Sun-asteroid direction, pointing outwards, the z-axis is along the direction of the angular momentum of the asteroid orbit, and the y-axis completes the right-hand system.

$$\begin{cases} \ddot{x} - 2\dot{y} = -\dfrac{x}{r^3} + 3x + \beta \\ \ddot{y} + 2\dot{x} = -\dfrac{y}{r^3} \\ \ddot{z} = -\dfrac{z}{r^3} - z \end{cases} \tag{20}$$

where x, y, and z are the non-dimensional particle positions with respect to the centre of the asteroid in the synodic frame, and $r = \sqrt{x^2 + y^2 + z^2}$ is the particle's distance from the centre of the asteroid. The lightness parameter β can be expressed as follows [14]:

$$\beta = \frac{P_0}{c}\frac{AU^2}{\frac{1}{\mu^3}\mu_{\text{Sun}}^{2/3}}\frac{3(1+c_{\text{R}})}{2\rho_{\text{p}}d_{\text{p}}} \tag{21}$$

where P_0 = 1367 W/m^2 is the solar flux at 1 AU, c is the speed of light, AU is the astronomical unit, μ_{Sun} and μ_a are the gravitational parameter of the Sun and the asteroid, respectively, ρ_p is the particle density, d_p the particle diameter, and C_r the reflectivity coefficient (here considered equal to the albedo of the asteroid). Eclipses are considered using a cylindrical shadow model via a modified lightness parameter, β^*:

$$\beta^* = \begin{cases} \beta & \text{if } x \leq 0 \\ \beta \cdot f(\sigma) & \text{otherwise} \end{cases} \tag{22}$$

where $f(\sigma) = (1 + e^{-s\cdot\sigma})^{-1}$ is a sigmoid function with steepness parameter s, which, in this work is equal to 8. The variable σ = r_x - R_a, with $r_x = \sqrt{y^2 + z^2}$ distance to the x-axis.

5.2 Sampling procedure

The sampling procedure objective is to obtain a set of weighted initial conditions. To each sample we associate a number of fragments, that we refer to as "representative fragments," n_r. In this way, each sample is also representative of an ensemble of fragments to have a better representation in space and time of the overall fate of the ejecta.

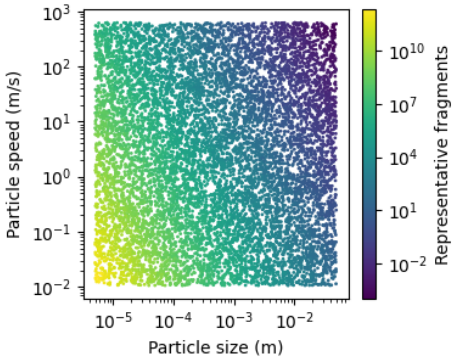

Figure 16: Example of sampling in the particle size vs ejection speed space. The colour represents the number of representative fragments associated to each sample.

To perform the sampling, we exploit the features of the ejecta distribution of Section 3. In fact, this is an analytical description based on a combination of conditional PDFs. Therefore, we can obtain the corresponding CDFs and integrate the distribution analytically within the desired ranges. However, we do not directly sample the distribution; indeed, this procedure will only cover a small portion of the state space as most of the sample will be concentrated towards very small particle radii. Instead, we want to characterise the entire domain as shown in Figure 16 for the particle size vs speed domain. To associate the weights to each sample, we subdivide the state space of initial conditions into a series of bins; we integrate the distribution inside these bins to get the total number of fragments associated with it. We then find the number of samples belonging to each bin. The representative fragments associated to the samples are then the total fragments of the bin divided by the number of samples. Therefore, for each bin, the representative fragments are equally distributed among the samples. For a more detailed description of the sampling procedure the reader is referred to [2].

In this work, we also distribute the number of samples we draw differently depending on the particle size range we consider. Specifically, to the range between 10 μm and 1 mm, we assign 70% of the samples, to the range between 1 mm and 1 cm we assign 25% of the samples, and to the range between 1 cm and 10 cm we assign 5%. Therefore, fi we draw a total of 1 million samples, 700 000 will be within 10 μm and 1 mm, 250 000 within 1 mm and 1 cm, and 50 000 within 1 cm and 10 cm.

The ejection speed is sampled up to the escape speed of the asteroid. The out-of-plane ejection angles, ψ, is sampled within ±3σ of the Gaussian distribution.

The binning for the computation of the representative fragments is the following: 10 bins in ejection speed, 36 in the in-plane ejection angle, ξ, 18 bins in ψ, and a total of 16 bins in particle diameter in logarithmic scale.

5.3 Flux estimation

The procedure for the computation of the flux first requires the estimate of the particle density and speed. The following procedure is used:

1. Draw the initial conditions as in Section 5.2, with the relevant representative fragments.
2. Propagate the samples using the desired dynamical model. In this work, we use the photo-gravitational Hill problem (Section 5.1).
3. Save the evolution of the cloud of fragments at specific snapshots in time. In this work we store the trajectory every 30 minutes.
4. Discretise the space around the asteroid with a spherical grid as in Figure 17.

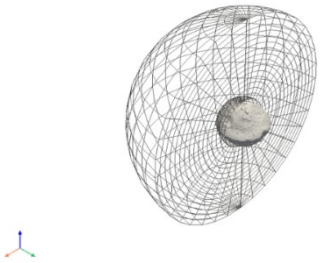

Figure 17: Example of spherical grid around asteroid Ryugu. The grid is cur along the x-z plane for better visualisation.

5. Estimate the fragments' density and speed inside each bin using the representative fragments. At each snapshot, in each bin we have:

$$\rho(r,\alpha,\delta) = \frac{\sum_i^{N_s} n_{r_i}(r,\alpha,\delta)}{\Delta V(r,\alpha,\delta)}$$

$$\boldsymbol{v}(r,\alpha,\delta) = \frac{\sum_i^{N_s} n_{r_i}(r,\alpha,\delta)\cdot \boldsymbol{v_i}}{\sum_i n_{r_i}(r,\alpha,\delta)}$$

Where $\rho(r, \alpha, \delta)$ is the estimated fragments density for a bin located at (r, α, δ), $\boldsymbol{v}(r, \alpha, \delta)$ is the weighted average velocity of the fragments inside the bin at (r, α, δ), N_s is the number of samples in the considered bin, n_{ri} is the representative fragments associated with the i-th sample in the bin and $\boldsymbol{v}_i$ is the velocity of the i-th sample in the bin. Figure 18 shows an example of the estimated density around the asteroid after 1 hour of propagation.

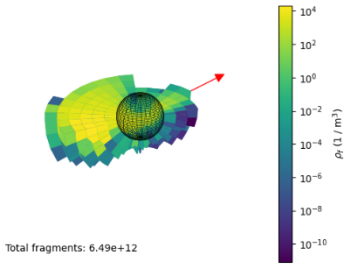

Figure 18: Spatial distribution of the estimated particle density around the asteroid at a snapshot in time. The volumetric representation is cut at the x-y plane for a better visualisation.

Once we have the information about the fragments' density and speed, we can compute the flux of particles or impact rate on a spacecraft passing through the cloud. Let us consider a spacecraft of cross-section A; at a certain instant in time, the spacecraft will occupy a position in space around the asteroid. This position will fall inside one of the spherical bins in which we have subdivided the space around the asteroid. When inside this bin, we consider that the spacecraft is affected by the fragments of density $\rho(r, \alpha, \delta)$, moving with average speed $\boldsymbol{v}(r, \alpha, \delta)$. Taking into account the spacecraft speed we can compute the impact rate of particles on the spacecraft, $\dot{\eta}_{sc}$, as follows:

$$\dot{\eta}_{sc}(r,\alpha,\delta) = \rho(r,\alpha,\delta) \cdot |(\boldsymbol{v}(r,\alpha,\delta) - \boldsymbol{v}_{sc})| \cdot A \qquad (23)$$

In time, the spacecraft will move through different spherical bins. We can compute the estimated number of impacts on the spacecraft with the following approximation:

$$N_{imp} \cong \sum_{t=1}^{N_T} \dot{\eta}_{sc}^{t}(r_t,\alpha_t,\delta_t)\cdot \Delta T_t \qquad (24)$$

Where N_T is the number of points in which the spacecraft trajectory is discretised. At this stage of development of the methodology, we consider that the spacecraft at time t is influenced by the fragments inside the bin it is occupying until the next point along its trajectory, t+1, for a time ΔT_t.

5.4 Test case

The test case we show is of an impact with characteristics as in Table 2 on asteroid Ryugu (Table 1). The material of the asteroid is assumed to be WCB, and the impact occurs at a location, expressed in the synodic frame, of 270° in right ascension and 0° in declination (see Figure 19). We test the computation of the impact rate and total number of impacts on a hovering spacecraft at different locations around the asteroid as show in Figure 19. The spacecraft is hovering in the synodic frame; therefore, it always occupies the sample spherical bin throughout the test. The spacecraft is assumed to be a sphere with cross-section of 1 m^2.

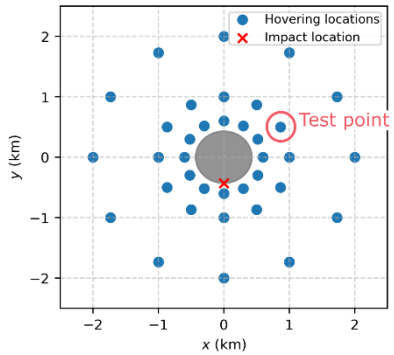

Figure 19: Hovering locations of the spacecraft (blue dots); test point (red circle); impact point (red cross).

5.5 Results

The analysis considers two type od sensitivities. A first test in which we look at the variability of the impact predictions as a function of the number of samples, and a second case, in which we analyse the stability of the sampling techniques by comparing different realisations (i.e., sampling of the initial conditions) with the same number of samples.

5.5.1 Sensitivity to number of samples

Three sets of samples are considered: 250 000, 500 000 and 1 million samples.

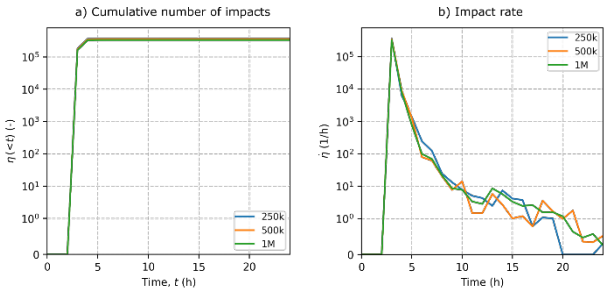

Figure 20: a) cumulative impact at the test point. b) impact rate evolution at the test point. The three different colours represent the number of samples used in the simulations.

Figure 20 shows the total number of impacts (a) and the impact rate (b) on the spacecraft at the test point highlighted in Figure 19. We observe that, at this location, the total number of impacts is well predicted in all three cases. The impact rate, instead, shows a smoother behaviour as the number of samples increases.

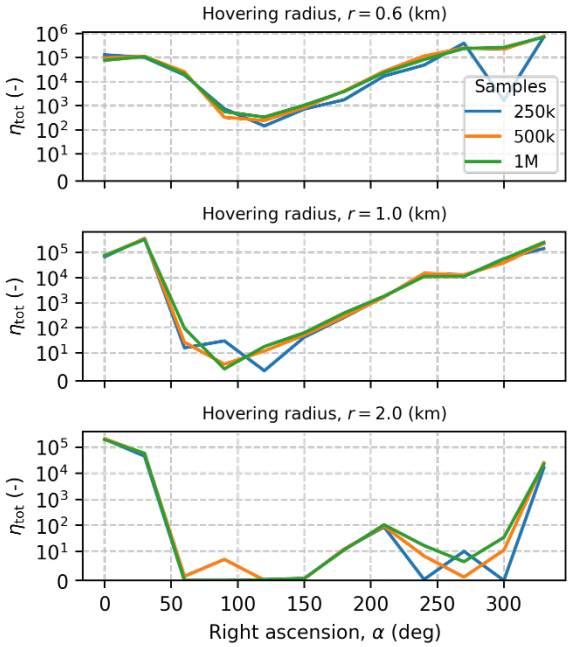

Figure 21: Total number of impacts at all the hovering locations. On the x-axis the right ascension of the hovering point. From top to bottom, increasing radial distances.

Figure 21 shows the same computation of Figure 20a for all the hovering locations of Figure 19 (blue dots). On the x-axis we have the right ascension of the test location, while from top to bottom we have the different radial distances, from 600 m to 2 km. We first observe a trend in the number of predicted impacts in all three cases. The highest number of impacts is predicted closer to the asteroid and for hovering locations on the antisolar side of the asteroid. We also observe that the prediction with the lowest number of samples is more unstable, while the ones with 500k and 1 million samples are in better agreement. In addition, the farther we move from the asteroid the less stable the predictions are. Two locations in right ascension show a higher variability that are the ones around the impact point (270°) and opposite to it (around 90°).

5.5.2 Sensitivity to different realisations

In this test, we perform 10 simulations, each one with 1 million samples. We look at the variability of the results as a function of the different realisations to check the stability of the predictions.

Similarly to Figure 20, Figure 22 shows the cumulative number of predicted impacts (a) and the impact rate (b) for a spacecraft placed a the test point highlighted in Figure 19. In this case, we show with a blue line the median of the realisations and the grey area shows the range inside the 5%-95% quantiles. Also in this case, we observe the stability of the prediction of the total number of impacts. The impact rate (b) instead shows higher variability after about 6 hours. The higher stability of the prediction of the total number of impacts is mainly due to the stability in the prediction of the high impact rate of small particles at the beginning. After the first stream of small particles passes, the predictions become more variable as lower number of samples are present around the asteroid. As the presented procedure is inherently statistical and is based on a discretisation in space and time, it is expected that it will more challenging to predict the fluxes at later stages.

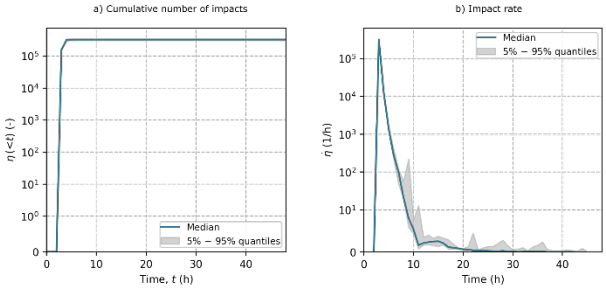

Figure 22: a) the cumulative number of impacts at the test point. b) the impact rate at the test point. In both plots, the blue line represents the median of the simulations and the grey shaded area the quantiles.

However, we can observe in Figure 23 that the prediction of the total number of impacts as a function of different realisations is quite stable among the different testing locations. As in the analysis of Section 5.5.1, the highest variability is observed at right ascension around 90° and 270°, with greater uncertainty around 90°. Nonetheless, in most cases, the order of magnitude of the amount of expected impacts is well captured making this methodology suitable for understanding what locations

could be selected to maximise the collection of samples in orbit around an asteroid.

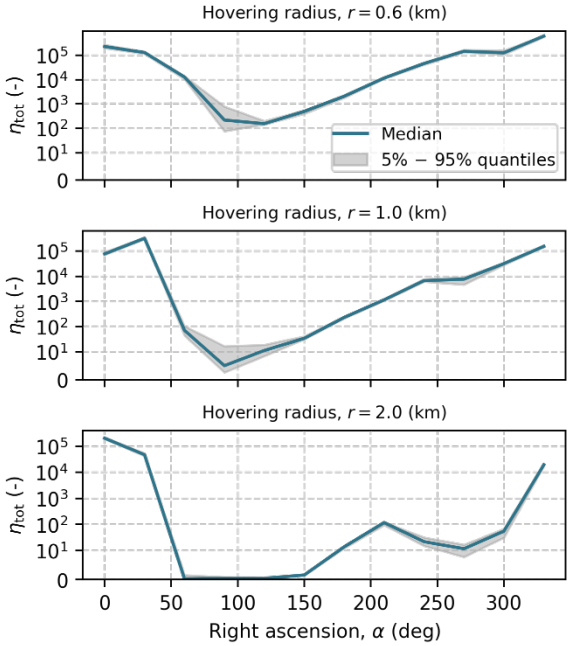

Figure 23: Total number of impacts at all the hovering locations. On the x-axis the right ascension of the hovering point. From top to bottom, increasing radial distances. The blue line is the median number of impacts, and the grey shaded area is the quantiles.

6. Conclusions and discussion

The presented work has been articulated in three different analyses, with different scopes and approaches.

The first analysis of Section 4.1 shows a preliminary study on the overall ejecta fate as a function of target and impactor properties as well as the type and strength of the material selected to model the target asteroid. From the results of Figure 4 to Figure 6, we can observe a few interesting features: the number of fragments quickly escaping or reaching only low altitudes varies significantly with the material type and strength. In this case, a substantial variation is observed passing from 10 to 1000 Pa of strength. However, this variation depends on the characteristics of the asteroid as it is linked to its escape speed. As shown in Figure 4c, there is still a large number of potentially collectable particles (at least in the order of billions) that have the potential for collection. This number increases with decreasing material strength. A similar trend can be observed when considering uncertainties in the impactor characteristics. In this case, however, a greater variation of the overall number of fragments is also observed (Figure 8) that is caused by the sensitivity of the impact crater size to the impactor speed. These analyses suggest that the fraction of fragments potentially available for collection is more influenced by the material type and strength than uncertainties in the target or impactor properties. However, changing some impactor properties can substantially affect the total number of ejected particles and, therefore, the amount of collectable particles as well.

The second analysis of Section 6, concerns the conditions for the fragments to reach quasi-stable orbits. We could observe interesting features from the results of Figure 14 and Figure 15:

- the sand-like material (Figure 14) does not generate fragments in quasi-stable orbits in a large central area from -45 to +45 deg of right ascension and up to 50 deg in declination. For this material, in fact, we assume an upper particle limit of 1 cm which is below the minimum required diameter for quasi-stable orbits from these impact regions.
- the WCB material instead has a 10 cm upper limit and allows quasi-stable orbits to be found. In addition, we have a slight asymmetry in the WCB plot (Figure 15), with a slightly higher number of fragments for negative α angles. This is due to the rotational contribution of Ryugu.
- the maximum number of fragments in quasi-stable orbits is for equatorial impacts and in the Sun's direction. However, these orbits have a shorter orbiting time.
- the maximum number of fragments is one order of magnitude larger for sand-like materials; however, the total ejected fragment from the crater is up to three orders of magnitude larger.

Therefore, we observe that quasi-stable orbits may be of interest for in-orbit sample collection. In fact, there is a non-negligible amount of particles potentially ejected into quasi-stable orbits, if the proper impact site is selected. In addition, these orbits have longer residence times; therefore, they allow for a less challenging mission design. Finally, they also show a low dependency upon the material type and strength, making it a potentially reliable target for in-orbit sample collection.

Finally, the third analysis of Section 8 has shown a methodology to estimate the number of collectable fragments as function of time and the position of the spacecraft around the asteroid. The methodology has been tested against numerical stability to assess its reliability in predicting the collectable samples. From Figure 20 to Figure 23 we can observe:

a. Number of samples
   - for the specific test point, the order of magnitude of the number of impacts is captured by all the simulations, despite the different amounts of samples.

- the impact rate behaviour is more stable as the number of samples increases.
- when looking at all tested locations (Figure 21), and the order of magnitude of the total number of impacts is mostly in agreement. However, some larger differences can be observed in certain regions and for the lowest number of samples.

b. Different realisations
- with different runs of the simulation, the total amount of collected particles is mostly stable (same order of magnitude), except for some regions
- these regions are the same as the previous analysis, indicating they are more challenging to predict.
- the impact rate behaviour also presents uncertainties. They are related to the difficulties in capturing continuous behaviour with an approach that is discretised in space and time.

This technique can be used for an overall estimate of the total number of impacts as a function of the collection location; therefore, it is useful to understand the most promising collection strategies.

Acknowledgements

This project has received funding from the European Union's Horizon 2020 research and innovation programme under the Marie Sklodowska-Curie grant agreement No 896404 – CRADLE.

References

[1] Trisolini M., Colombo C., Tsuda Y. (2021). Ejecta analysis for an asteroid impact event in the perturbed circular restricted three body problem, *31st JAXA Workshop on Flight Mechanics and Astrodynamics*, Virtual, 26-27 July 2021.

[2] Trisolini M., Colombo C., Tsuda Y., Ejecta models for particles generated by small kinetic impactors onto asteroid surfaces, *AIAA SciTech Forum 2022*, AIAA 2022-2383, DOI: 10.2514/6.2022-2383.

[3] Trisolini M., Colombo C., Tsuda Y. (2021). Ejecta dynamics around asteroids in view of in-orbit particle collection missions, *Proceedings of the International Astronautical Congress,* Dubai, UAE.

[4] Watanabe, S., Hirabayashi, M., Hirata, N., Hirata, N., Noguchi, R., Shimaki, Y., ... & Tsuda, Y. (2019). Hayabusa2 arrives at the carbonaceous asteroid 162173 Ryugu—a spinning top–shaped rubble pile. Science, 364(6437), 268-272.

[5] Arakawa, M., Saiki, T., Wada, K., Ogawa, K., Kadono, T., Shirai, K., ... & Miura, A. (2020). An artificial impact on the asteroid (162173) Ryugu formed a crater in the gravity-dominated regime. *Science*, *368*(6486), 67-71.

[6] Housen, K. R., & Holsapple, K. A. (2011). Ejecta from impact craters. *Icarus*, *211*(1), 856-875.

[7] Holsapple, K. A., & Housen, K. R. (2007). A crater and its ejecta: An interpretation of Deep Impact. *Icarus*, *191*(2), 586-597.

[8] Holsapple, K. A., & Housen, K. R. (2012). Momentum transfer in asteroid impacts. I. Theory and scaling. *Icarus*, *221*(2), 875-887.

[9] Yu, Y., & Michel, P. (2018). Ejecta cloud from the AIDA space project kinetic impact on the secondary of a binary asteroid: II. Fates and evolutionary dependencies. *Icarus*, *312*, 128-144.

[10] Sachse, M., Schmidt, J., Kempf, S., & Spahn, F. (2015). Correlation between speed and size for ejecta from hypervelocity impacts. *Journal of Geophysical Research: Planets*, *120*(11), 1847-1858.

[11] Yu, Y., Michel, P., Schwartz, S. R., Naidu, S. P., & Benner, L. A. (2017). Ejecta cloud from the AIDA space project kinetic impact on the secondary of a binary asteroid: I. mechanical environment and dynamical model. *Icarus*, *282*, 313-325.

[12] Richardson, J. E., Melosh, H. J., Lisse, C. M., & Carcich, B. (2007). A ballistics analysis of the Deep Impact ejecta plume: Determining Comet Tempel 1's gravity, mass, and density. *Icarus*, *191*(2), 176-209.

[13] Scheeres, D. J., & Marzari, F. (2002). Spacecraft Dynamics in the Vicinity of a Comet. The Journal of the astronautical sciences, 50(1), 35-52.

[14] Scheeres, D. J. (2012) Orbital Motion in Strongly Perturbed Environments - Applications to Asteroid, Comet and Planetary Satellite Orbiters, Springer-Verlag Berlin Heidelberg. DOI:10.1007/978-3-642-03256-1

[15] Richter, K., & Keller, H. U. (1995). On the stability of dust particle orbits around cometary nuclei. Icarus, 114(2), 355-371.

[16] Scheeres, D. J., & Marzari, F. (2000). Temporary orbital capture of ejecta from comets and asteroids: Application to the Deep Impact experiment. Astronomy and Astrophysics, 356, 747-756.

[17] Carry, B. (2012). Density of asteroids. *Planetary and Space Science*, *73*(1), 98-118.